

INTEGRATION OF A SOLID OXIDE FUEL CELL PROPULSION SYSTEM: A TECHNOLOGY DEVELOPMENT GOAL FOR REGIONAL AIRCRAFT

Nicolas Schneiders[1], Dennis Keller[2], Antje Link[3], Tim Burschyk[1] & Georgi Atanasov[1]

[1]German Aerospace Center (DLR), Institute of System Architectures in Aeronautics, Hamburg, Germany
[2]German Aerospace Center (DLR), Institute of Aerodynamics and Flow Technology, Brunswick, Germany
[3]German Aerospace Center (DLR), Institute of Electrified Aero Engines, Cottbus, Germany

Abstract

Solid Oxide Fuel Cells (SOFCs) offer high potential for aircraft propulsion. They promise a higher efficiency than Polymer Electrolyte Membrane Fuel Cells (PEMFCs) and operate at significantly higher temperatures. While PEMFC powertrains face challenges in designing their thermal management system to manage their waste heat, within SOFC powertrains the focus shifts to a thorough conditioning system design instead. The technology readiness level of SOFCs with regard to mobile applications, however, needs to be improved to become applicable for aviation. This study derives a development goal for SOFC concerning its gravimetric power density. Therefore, the integration of an SOFC propulsion system into a regional aircraft in the category of 50 passengers is investigated on overall aircraft level. A multidisciplinary design analysis is conducted combining a conceptual aircraft design tool and mid-fidelity simulation codes for critical technologies and disciplines, e.g. the SOFC-powertrain sizing. Two integration configurations are designed and analyzed: one with the SOFC system integrated into the aircraft's nacelles and one into the fuselage. Additionally, computational fluid dynamics analyses assess the influence of the different nacelle sizes on the aerodynamic performance. A design study regarding the SOFC's gravimetric power density identified a minimum requirement of 450 W/kg on stack level to be achieved in order to compete with an evolutionary advanced conventional regional aircraft for the year 2050.

Keywords: Aircraft Design, Regional Aircraft, Solid Oxide Fuel Cell, Technology Integration, Computational Fluid Dynamics

1. Introduction

Polymer Electrolyte Membrane Fuel Cells (PEMFCs) are the most extensively researched fuel cell technology for aircraft propulsion. PEMFCs are already tested on regional aircraft as retrofit shown by Universal Hydrogen and ZeroAvia [1]. State of the art PEMFCs achieve a gravimetric power density of about 2.5 kW/kg on stack level [2] and show good dynamic behavior [3]. However, their low operating temperature of about 80 °C necessitates a large and heavy thermal management system since less heat transfer is possible via sole temperature difference to the ambient. This is especially true for low-temperature PEMFCs (LT-PEMFCs). Another challenge with LT-PEMFCs is the water management. Depending on the power demand, dehydration of the membrane-electrolyte assembly or electrode flooding may occur. This needs to be counteracted which adds weight to the system [1]. Furthermore, LT-PEMFCs rely on expensive catalyst materials such as platinum [4] which show low tolerances to impurities within the fuel [1, 3].

One promising alternative to PEMFCs can be Solid Oxide Fuel Cells (SOFCs). SOFCs operate at significantly higher temperatures which can simplify its integration. Moreover, they promise higher efficiencies than PEMFCs in spite of the lower technology readiness level for mobile applications.

Marciello et al. [5] state that an SOFC-powered regional aircraft has the highest fuel energy reduction potential compared to an aircraft powered by PEMFCs or direct combustion in the timeframe 2045 onwards. Furthermore, SOFCs show higher fuel flexibility through internal reforming [1] and more tolerance to impurities possible due to different materials used. For example, nickel is incorporated as electrocatalysts instead of platinum [1, 3, 6]. Nevertheless, there are still challenges with SOFCs that require further research. Depending on the scope of a regarded study in the literature, the values for the gravimetric power density of an SOFC vary considerably. Current SOFC assemblies show a low gravimetric power density of about 0.1 kW/kg [7]. Assumptions for the mid 2020s come to about 0.2 - 0.3 kW/kg on stack level [2, 6]. However, laboratory-scale studies show potential for an SOFC gravimetric power density of up to 2.5 kW/kg on stack level [8]. Tew et al. [9] state a target gravimetric power density of 0.7 kW/kg for an SOFC to be viable for a commercial singe aisle aircraft. Other challenges for the application of SOFCs in aviation are the rather long start-up times and the inferior dynamic behavior compared to PEMFCs and other propulsion options [3]. A comparison of current state of the art properties of LT-PEMFCs and SOFCs are listed in Table 1.

LT-PEMFC	Property	SOFC
1.5 ... 3 kW/kg	Power density [2, 6, 7]	0.1 ... 0.3 kW/kg
60 ... 90 °C	Operating temperature [3]	650 ... 1000 °C
1 ... 3 bar	Operating pressure [1]	1 ... 10 bar
good	Dynamic operation [3]	difficult
40 ... 60 %	Efficiency potential [3]	60 ... 65 %
low	Tolerance for fuel impurities [1, 3]	high
No	Fuel flexibility [1]	Internal reformation
platinum	Catalyst material [3]	nickel

Table 1 – Comparison of LT-PEMFC and SOFC at current state-of-the-art.

Previous studies on SOFC applications for aircraft have treated this type of fuel cell as a subsystem designed to replace the auxiliary power unit (APU), or have focused on supplying electrical power to on-board systems throughout the mission [10, 11]. Here both come to the conclusion that pressurizing inlet air is advantageous for the efficiency of SOFC. Optimum performance for an APU replacement occurs at 8 atm according to [10]. Santarelli et al. [11] also state that higher SOFC masses can be offset by higher efficiencies of the SOFC through the use of its excess heat and thereby the omission of bleed air from the engine which increase the efficiency of the engine as well. Seitz et al. [12] state that gas turbine efficiency can be improved by steam injection using the waste water of the fuel cell. According to this study, only the use of SOFCs showed an opportunity for fuel savings, while PEMFCs do not lead to fuel reductions in the short- and medium range sector.

Other studies investigate a gas turbine hybridization with SOFCs in different layouts: Waters and Cadou [13] proposed a parallel hybrid consisting of classical gas turbine and SOFCs. Here, the combustion chamber and the SOFCs are placed in parallel, both using the pressurized air form the compressor and releasing their heat to the same turbine. The SOFCs generate electricity and replace the turbo generator of the classical gas turbine. Thereby relieving load from the gas turbine and reducing fuel burn. Collins and McLarty [14] propose an all-electric propulsion for narrow and wide-body aircraft. Air is compressed and fed to the SOFCs which produce electricity. Excess heat of the fuel cells is released in a turbine powering a generator. A battery buffers additional power demand during take-off. All sources of electricity power electric motors. This architecture omits the combustion chamber. In the architecture of Köhler et al. [15] an additional combustion chamber is introduced after the SOFCs using excess hydrogen and increasing the electrical output from the turbine. However, a battery is omitted. This architecture is targeted for a regional class aircraft. Lastly, Kierbel et al. [16] regard the use of SOFCs on aircraft level in the short and medium range sector, showing the interest of the aviation industry regarding this propulsion technology.

Given the potential benefits of the SOFC technology compared to LT-PEMFCs, the goal of this paper

is to evaluate the possibility of utilizing an SOFC powertrain in a regional aircraft in the category of 50 passengers. Thereby, the SOFC is used as primary power provider whose heat is released in a turbine. The system is buffered by a battery. Hence, combining Collins and McLarty's as well as Köhler et al.'s approach. Furthermore, two powertrain architectures are evaluated: one for the integration into the aircraft's nacelles and one for the integration into the fuselage.

The next sections describe the methodology of how the aircraft incorporating the SOFC powertrains are designed including the assumptions for the powertrain and design choices made. Thereafter the results are presented. The SOFC-powered aircraft are described in detail including a comparison with an evolutionary advanced conventional regional aircraft for the year 2050. The paper concludes with a sensitivity analysis regarding the gravimetric power density assumption of the SOFC in order to derive a development goal for long-term application of this technology.

2. Methodology

This section covers the aircraft design process. The calculation routine to establish the SOFC-powered aircraft is shown. Thereby, a baseline is introduced, which is an aircraft of comparison for the SOFC-powered aircraft. Moreover, the design choices and assumptions leading to the aircraft concepts incorporating an SOFC powertrain are outlined.

2.1 Aircraft design process

The aircraft design process consists of sequential calculation routines of different disciplinary tools built as a workflow within the Remote Component Environment (RCE) [17]. For data exchange between the tools the Common Parametric Aircraft Configuration Schema (CPACS) [18] is used. The workflow is initiated by defining top-level aircraft requirements (TLARs) and design parameters as input, such as assumptions regarding the technology under investigation. The overall aircraft sizing is performed by the tool *openAD* [19] which is based primarily on empirical and semi-empirical methods. The *engine deck generation* lays the foundation for the mission analysis by calculating altitude, speed and thrust combinations based specifically on efficiencies of the SOFC-powertrain components and the propeller. A linear correlation between the powertrain efficiencies during takeoff, climb, cruise, and descent phases is assumed. The *aircraft mission calculator* (AMC) computes the trajectory and provides flight performance data by solving the equation of motion for every timestep of a specified mission. The trajectory from AMC is subsequently employed by the *powertrain sizing* which generates masses and volumes of the SOFC-powertrain components as well as the power consumption and required fuel mass. Hereby, the powertrain sizing tool previously used by Bahrs et al. [20] has been adjusted with an interface to the overall aircraft sizing via CPACS to allow integration into the workflow, as well as an updated powertrain architecture that considers the SOFC-powertrain concepts and their specific components instead of a PEMFC-based powertrain. The *hydrogen-storage sizing* is an advancement of the liquid hydrogen (LH_2) storage sub-process by Burschyk et al. [21] including carbon fibre reinforced plastics (CFRP) as structural material [22]. In the concluding *synthesis*, the results of the tools are consolidated and fed back to the input of openAD to generate a more sophisticated aircraft design. After convergence is reached, the post-processing is conducted. Here, a *weight-and-balance* (WAB) analysis is included to check the center of gravity (CoG) shift and the *payload-range* characteristic is calculated. The entire sizing workflow for the SOFC-powered aircraft is shown in Figure 1.

As the electrical energy generated by the SOFC system is transmitted to the propellers via electric motors, a distributed propulsion (DP) configuration was selected for both powertrain integration concepts, motivated by the low size-sensitivity of electric motor performance. However, this approach adds complexity from an aerodynamics point-of-view as the nacelle size depends on the integration concept. Therefore, a computational fluid dynamics (CFD) study examined the aerodynamic performance, in particular with regard to the influence of the nacelle size. The *CFD analyses* were conducted once for an intermediate aircraft design for both powertrain integration concepts. The results of the CFD analyses serve as input for openAD to calibrate its aerodynamics methods.

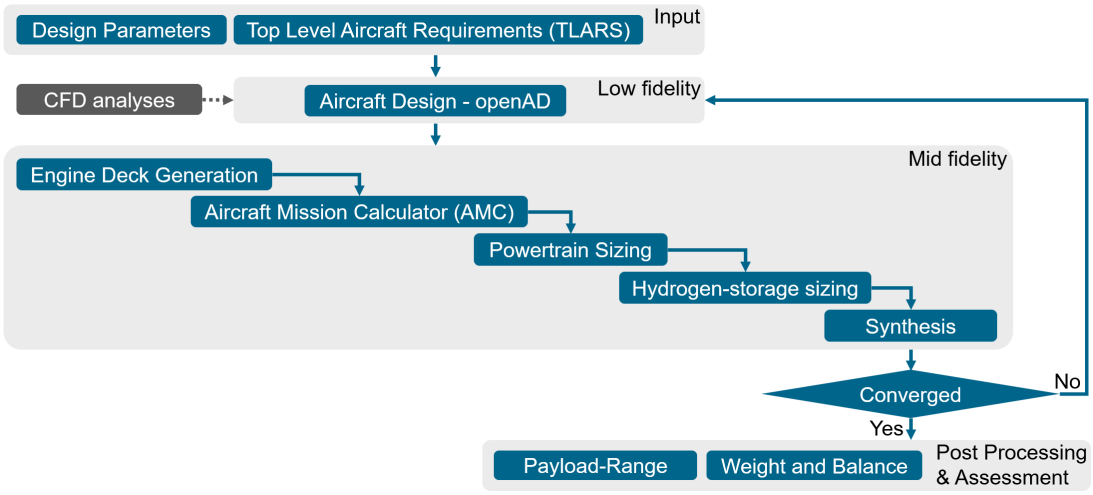


Figure 1 – Aircraft design workflow.

2.2 CFD analysis method

In order to assess the aerodynamic and propeller performance, numerical simulations based on the Reynolds-averaged Navier-Stokes (RANS) equations have been carried out with the *DLR TAU* code [23]. The code relies on an unstructured finite volume approach for solving the RANS equations. For the present investigation, the implicit LU-SGS scheme is used for time stepping and a central scheme and second order Roe upwind scheme for the spatial discretisation of the inviscid mean flow fluxes and the turbulent convective fluxes, respectively. The turbulence effects are modeled with the Spalart-Allmaras formulation (SA) [24] with vortical and rotational flow correction based on the Spalart-Shur correction [25]. The propeller effects are introduced into the computational domain by actuator disk boundary conditions based on 2D blade element momentum theory. In this way, the local forces of the propellers are calculated based on the blade properties and the local flow conditions. The blade properties are thereby given by radial distributions of the local chord length and twist as well as aerodynamic data sets reflecting the dependence of the local blade force coefficients on the angle of attack. The time averages of the resulting axial and normal forces are then imposed on the numerical domain of the RANS computation. Moreover, the forces are used to compute the integral values T, C_T, C_P, and the propeller efficiency η_{prop}. Detailed information on the actuator disk implementation can be found in [26, 27]. The actuator disk model has shown robust behavior and good results in terms of performance parameters (C_T, C_P) as well as slipstream velocity distributions – axial and circumferential – for various applications such as the simulations of conventional propellers [28] and contra-rotating open rotors [29].

2.3 Study Approach

The generation of a reference aircraft is a crucial first step in aircraft design. The selection is based on the availability of data, the similarity of mission requirements and the defined TLARs for the aircraft to be developed. The main purpose of the reference aircraft is to calibrate the models and tools. In this study an ATR 42-500-like aircraft is generated and validated against available data for size, mass and performance. Therefore, a trimmed-down workflow consisting of input, openAD, AMC, synthesis and post-processing is applied. openAD is calibrated in terms of overall geometry, masses, center of gravity and engine performance. The openAD-internal calculation for conventional gas turbines is applied to generate the engine deck for AMC which then calculates the fuel consumption in flight and thus payload-range performance. Figure 2 shows a three-side view of the generated aircraft and Figure 3 the payload-range matching with the data from [30].

Based on the reference aircraft, a baseline is derived which is an evolutionary advanced aircraft model for the year 2050 powered by gas turbines with hydrocarbon fuels. The same workflow and tools used for the reference aircraft are used to establish the baseline. The technology factors on structural mass, aerodynamic efficiency and gas turbine efficiency applied to the baseline compared

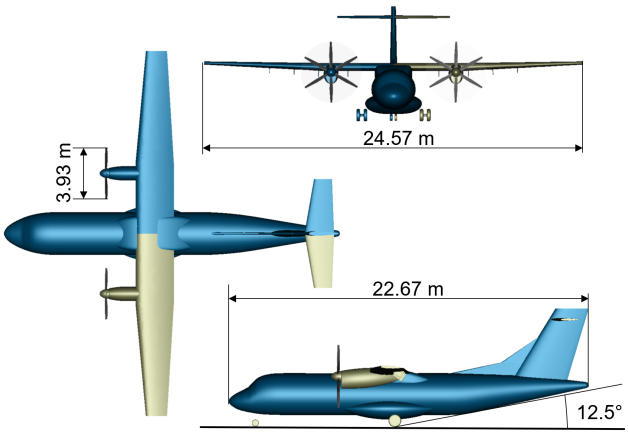


Figure 2 – Reference aircraft three-side view.

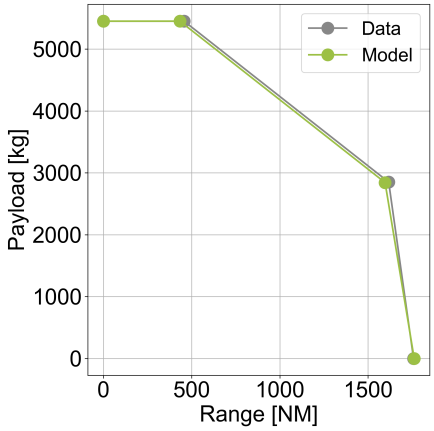


Figure 3 – Payload-Range matching.

to the reference are stated in Table 2. The main improvements come from better aerodynamics and higher engine efficiency. The competitiveness of existing regional aircraft depends more on airframe production and maintenance costs than on fuel efficiency. The overview in [30] indicates that in 2005 the fuel cost of an ATR 42 amounted to only about 10 % of the operating costs, whereas aircraft purchase and airframe maintenance costs weigh over 70 % of the total costs. Some of the technology factors in the study are based on the premise that in 2050 energy costs will be higher and high-quality manufacturing costs will be lower, which would allow producing a more efficient aircraft (e.g. lighter, better quality surface, less excrescences, more complex 3D surface contours etc.) and still remain competitive on the market. The corresponding parasitic drag reduction assumption in Table 2 is only a rough estimate of this tendency and not a result from the analysis of the actual quality of the reference aircraft. The aerodynamic modelling of both the baseline and the concept aircraft is affected to a similar extend by this assumption, which means that the impact on their comparison in the results is low.

Parameter	Assumption 2050
Wing mass	-10 %
Empennage mass	-10 %
Fuselage mass	-5 %
Landing gear mass	-5 %
Parasitic drag (C_{D0})	-15 %
Gas turbine efficiency	+15 %

Table 2 – Technology factors for the baseline.

Following on from that, also engine improvements focus more on increasing the time-on-wing and reducing maintenance costs than on efficiency. Hence, the rather conservative assumption of 15 % gas turbine efficiency improvement by 2050 compared to current engines powering regional aircraft like the PW127. Furthermore, it is assumed that the propeller diameter would remain constant compared to the reference aircraft. However, the number of blades increased from six to eight to align with the already proposed ATR Evo concept for the mid 2030s [31]. The aspect ratio is increased to 14 to better align with current aircraft design trends for the market around the year 2050. The resulting wing span remains within the typical range for comparable aircraft. By 2050, it is expected that an ATR 42-like aircraft will be equipped with a fly-by-wire control system, which will replace the mechanical control via cables and rods and render horn-balanced control surfaces obsolete. Also, the design cruise Mach number is reduced from 0.48 to 0.4 to match the TLARs of the SOFC-powered aircraft. The baseline serves as comparison for the SOFC-powered concepts and is depicted in Figure 4. Its key data are stated in Table 3.

Figure 5 provides an overview of the impact on block energy of the individual assumptions in Table 2 for the baseline aircraft compared to the reference. The structural mass improvements for wing, empennage, fuselage and landing gear are summarized as lighter airframe and achieve a 2 % block fuel reduction. The two major improvements result from the assumed advancements in engine efficiency and aerodynamic performance with 12 % and 13 %, respectively. Also, the reduction in cruise Mach number from 0.48 to 0.4 leads to a reduction of 9 % in block fuel consumption. The overall block

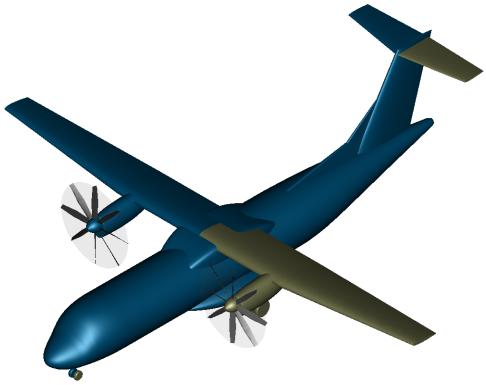


Figure 4 – Baseline aircraft ISO view.

Parameter	Unit	Value
MTOM	kg	16645
OEM	kg	10295
PAX	-	48
Max. Payload	kg	5450
Fuselage length	m	22.67
Wing area	m^2	54.6
Wing span	m	27.6
Aspect ratio	-	14
Design Range	NM	840
Cruise Ma	-	0.4
Cruise altitude	ft	24000
L/D mid cruise	-	17.4

Table 3 – Key data of the baseline aircraft.

fuel reduction from reference to baseline amounts to 36 %. This shows that there is already a high potential of improvement in the class of regional aircraft. The respective outcome stated in Figure 5 do not equal the assumptions in Table 2 which is the nature of showcasing individual improvements in succession where one improvement is based on the one before, e.g. the block fuel reduction due to improved engines is based on the aircraft already improved by the lighter airframe which results in less relative block fuel reduction compared to the assumptions stated in Table 2.

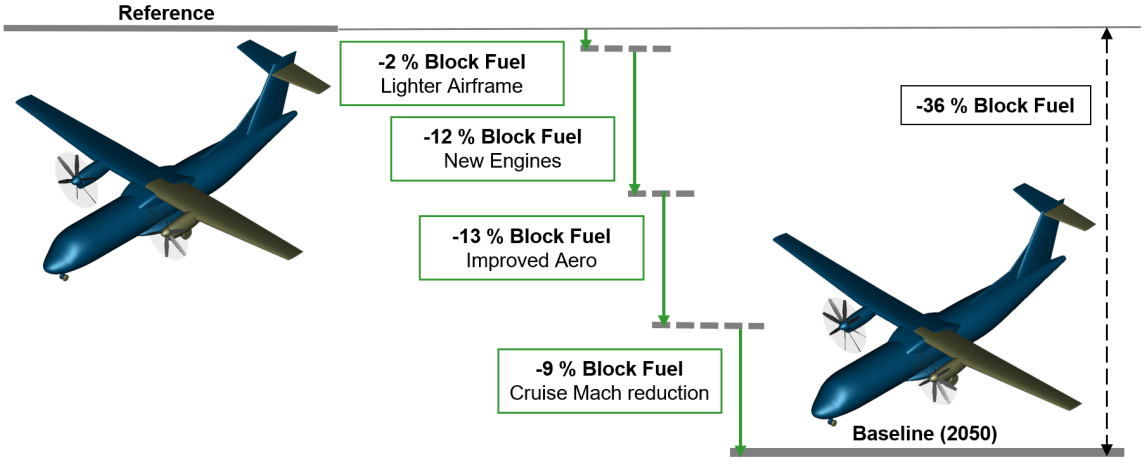


Figure 5 – Block energy reduction from reference to baseline aircraft.

For the aircraft incorporating an SOFC propulsion system, the general powertrain architecture as provided in Figure 6 is applied. Electric motors coupled via gearboxes drive the propellers. Further components within the electric drive train (EDT) considered during the sizing are the according power electronics, cables, circuit breakers and a liquid cooled thermal management system ensuring a constant operating temperature of the electric components throughout the mission. The power for the EDT is supplied by an SOFC system using liquid hydrogen as well as a battery in a parallel hybrid configuration. Within the modelling, the SOFC stack power is maintained at a fairly constant output throughout the mission while the battery addresses load changes by supplying peak power demands during take-off and climb, and capturing excess power from the SOFC during descent. In the synthesis of the workflow for the SOFC-powered aircraft, an additional dynamical adaptation of the hybridization between SOFC and battery is implemented. This ensures two things: First, during cruise no battery power is used which keeps the mass of the battery as low as possible. Second, at the end of the specified mission, the battery is charged again to about 100 %. This facilitates the comparison of the energy requirements of the different aircraft, since the energy consumed by the

battery during the mission balances out, and only the energy from the hydrogen consumed needs to be taken into account.

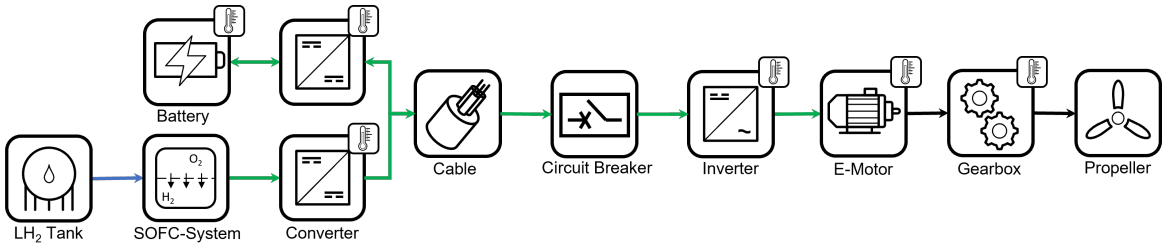


Figure 6 – Overall powertrain architecture.

For the SOFC system two different concepts are considered based on integration space assumptions: a nacelle-integrated concept and a fuselage-integrated concept. For the nacelle-integrated system, the EDT and the SOFC system are located within the nacelles while only the hydrogen storage as well as the battery and its converter are located within the fuselage. For the fuselage-integrated concept, only the EDT is located within the nacelles, while the SOFC system is located within the aircraft's fuselage. For the subsequent assessments, the following general assumptions have been taken from literature:

- SOFC stack gravimetric power density: 2.5 kW/kg [8]
- SOFC operating conditions: 1073.2 K (800 °C), 0.8 MPa (8 bar)
- Battery pack gravimetric specific energy: 500 Wh/kg [32] - conservative scenario.

The regarded mission for the SOFC-powered aircraft is depicted in Figure 7. This mission is based on the design mission for the ATR 42-600 [33]. The main mission reaches 740 NM of range at a cruise altitude of 24000 ft with a cruise Mach number of 0.4. The diversion distance is set to 100 NM.

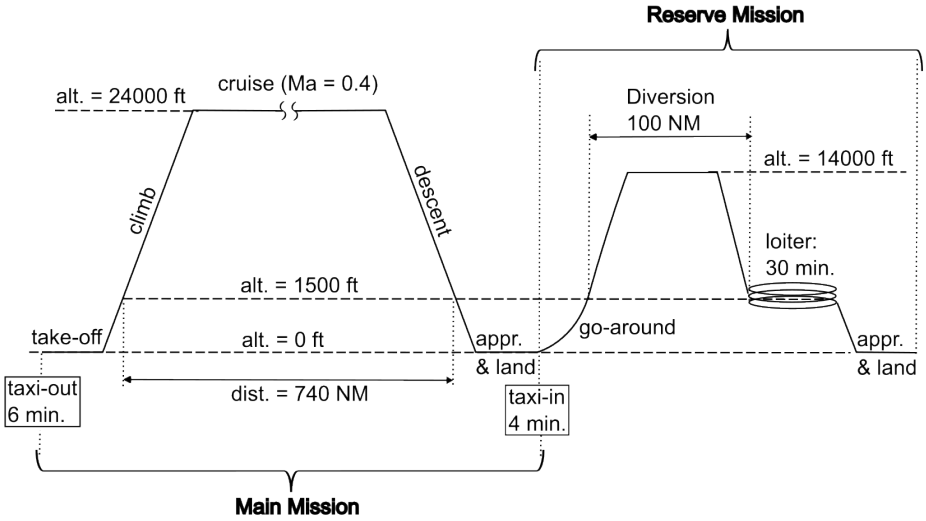


Figure 7 – Design mission.

3. Results

In this section, the results of the workflow described in the previous section are shown. First, the two SOFC aircraft configurations together with their powertrain architecture and integration are addressed. Followed by a detailed comparison of these aircraft among each other and with the baseline

concerning mass, weight and balance, aerodynamics, mission performance and block energy consumption. This section is concluded by a sensitivity analysis concerning the gravimetric power density of the SOFC stack for the more promising SOFC aircraft

3.1 Nacelle-Integrated Configuration

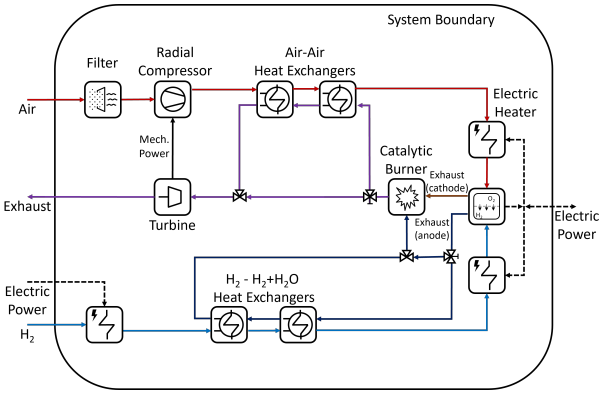


Figure 8 – SOFC system architecture of the nacelle-integrated concept.

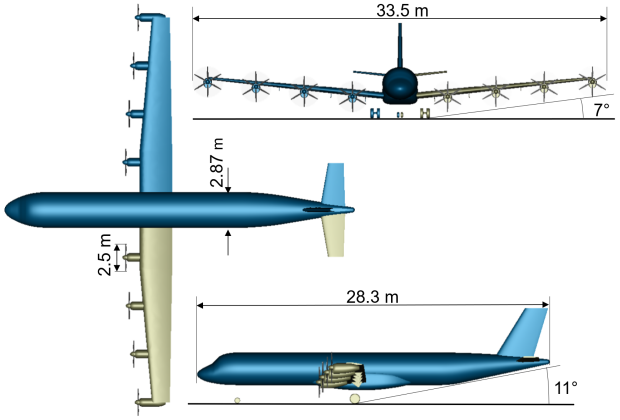


Figure 9 – Three-side view of the nacelle-integrated concept.

The SOFC system architecture for the nacelle-integrated (NI) concept is shown in Figure 8. The focus during the definition of the architecture was on reducing complexity, required parts and volume due to the intended nacelle integration. As system boundary for the hydrogen system, it is assumed that the hydrogen has been extracted from the tank and is provided in gaseous form at an appropriate pressure to achieve 8 bar at the SOFC stack. Within the SOFC system, the hydrogen is preheated initially in an electric heater close to the LH_2 tank to achieve non-cryogenic operating conditions for the hydrogen transport to the nacelles. Here, the hydrogen is further conditioned with the anode exhaust gas from the SOFC, consisting of excess hydrogen and water vapor. Further conditioning as well as heating during start-up is possible via an electric heater close to the SOFC. Ambient air is filtered and compressed via a radial compressor to achieve the operating pressure of 8 bar at the entry to the SOFC stack. The air is preheated in a cascade of two heat exchangers after compression to ensure a constant SOFC entry temperature throughout the mission. An additional electric heater serves for finetuning the temperatures before entering the SOFC stack. This electric heater also provides a means to support achieving the operating temperature of the SOFC during start-up on ground. Both fluid exhausts are interconnected by a catalytic burner to combust any excess hydrogen after the SOFC. This exhaust gas is used as conditioning medium for the air side heat exchangers. For energy recovery a turbine is employed that is directly mechanically coupled to drive the radial compressor used for compression on the air side.

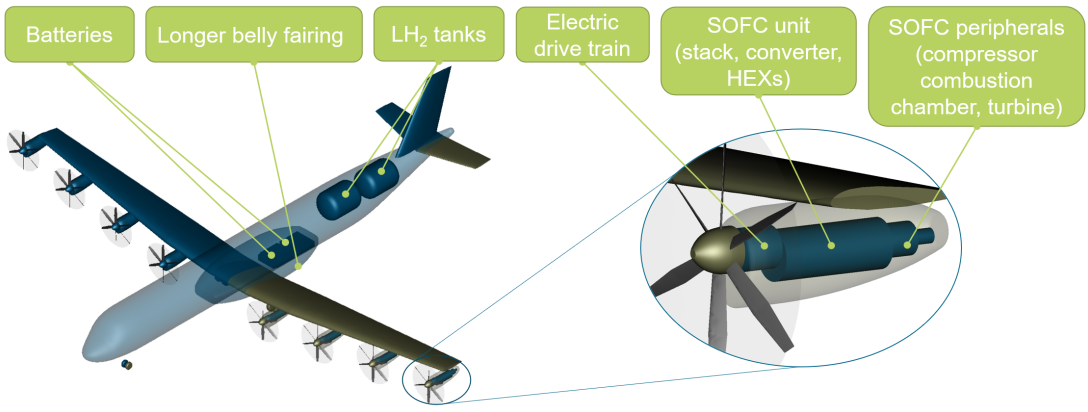


Figure 10 – Powertrain integration for the nacelle-integrated configuration.

Figure 9 shows a three-side view of the nacelle-integrated aircraft concept. The baseline's high-wing configuration has been replaced by a low-wing configuration. A high-wing configuration with heavy nacelles results in a landing gear that cannot be integrated into a reasonably sized belly fairing. A low-wing configuration significantly facilitates the integration of the landing gear and avoids an increase in fuselage mass due to the heavy wing, the weight of which would have to be transferred from the fuselage structure to the landing gear. Furthermore, compared to the baseline aircraft, the aspect ratio is kept constant. Nonetheless, the wing area increases to generate more lift due to a heavier aircraft which results in an increased span. The fuselage is lengthened to incorporate the hydrogen tanks in the rear. The diameter, however, remains unchanged from the baseline. For redundancy purposes, two hydrogen tanks are integrated into the aircraft's design. These tanks are identical in size, structure, and maximum operating pressure, reflecting the fact that the design of regional aircraft is driven more by cost considerations than by efficiency. The powertrain integration for the NI-concept is depicted in Figure 10. The batteries are located in the belly fairing which itself is lengthened compared to the baseline to also accommodate the fuel lines from the tanks to the nacelles. The nacelles in turn contain the electric drive train and the SOFC system. The SOFC unit consisting of stack, converter and heat exchangers is encapsulated in a pressure vessel. The remaining peripherals of the SOFC system are located behind that pressure vessel. This arrangement of components is identical in all eight nacelles. The key data of this aircraft configuration are given in Table 4.

3.2 Fuselage-Integrated Configuration

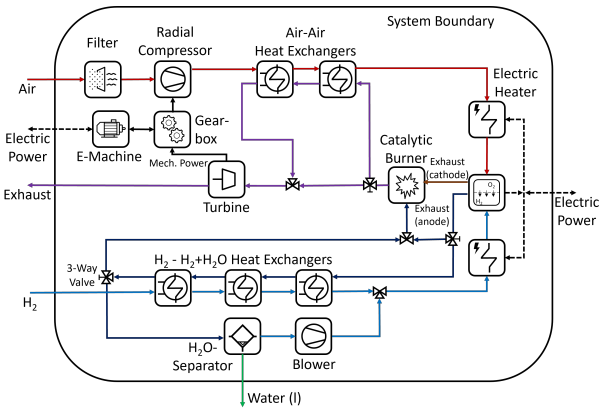


Figure 11 – SOFC system architecture of the fuselage-integrated concept.

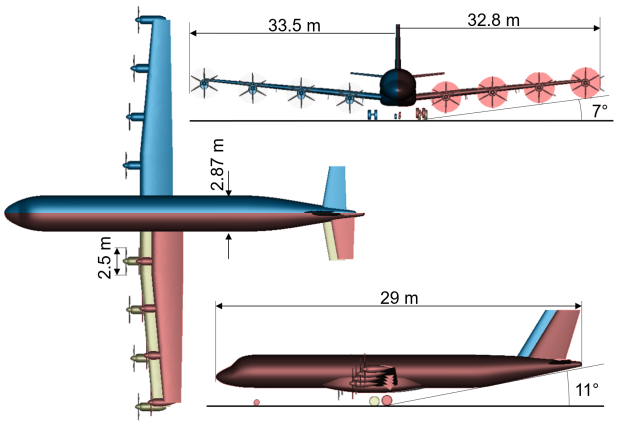


Figure 12 – Three-side view of the FI-concept (red) in overlay with NI-concept (blue).

The SOFC system architecture for the fuselage-integrated (FI) concept is depicted in Figure 11. While the basis of the architecture is very similar to the NI-concept, more focus was put on overall powertrain efficiency, i.e. more energy recovery while at the same time constraints of the volume were deemed less important compared to the NI-concept. On the cathode air side, the main difference occurs in the handling of the exhaust gas within the turbine. While the NI-concept was limited to a power recovery driven by the compression system, the FI-concept decouples the compressor and turbine mechanically through a gearbox. This enables the use of an electric machine, running in either motor mode to supply additional power in case the turbine output is insufficient to drive the compressor, or in generator mode to draw additional power for propulsion. Hence, load on the SOFC is relieved, resulting in lower fuel consumption. On the hydrogen side, the electric heater close to the tank within the NI-concept is replaced with a conventional heat exchanger, expanding the heat exchanger cascade to three connected heat exchangers. Furthermore, a recirculation of the excess hydrogen is considered instead of supplying all of the anode exhaust gas to the catalytic burner directly. This requires additional components such as a water separator to extract the liquid water and a further blower to maintain pressure within the system.

Figure 12 illustrates an overlay of the three-side view of the fuselage-integrated configuration superimposed on the one of the nacelle-integrated configuration. The comparison of the two aircraft

concepts reveals a high degree of similarity. The number of propellers and their diameter as well as the fuselage diameter are identical. The overall length of the FI-configuration is greater than the one of the NI-configuration due to the SOFC-powertrain integration into the fuselage. The wing area and span, however, are smaller for the FI-concept. This comes from the fact that the FI-concept is more lightweight than the NI-concept. Therefore, less lift needs to be generated. Concerning the wing position with respect to the baseline, the same design decision as for the NI-configuration was made, although landing gear integration was not the driving factor. Nevertheless, the decision was also taken in this configuration to avoid the additional mass of the fuselage by using a high-wing layout. This decision simplifies the comparison of the two configurations. The key data of the aircraft is stated in Table 4. A more detailed mass comparison is given in the next section.

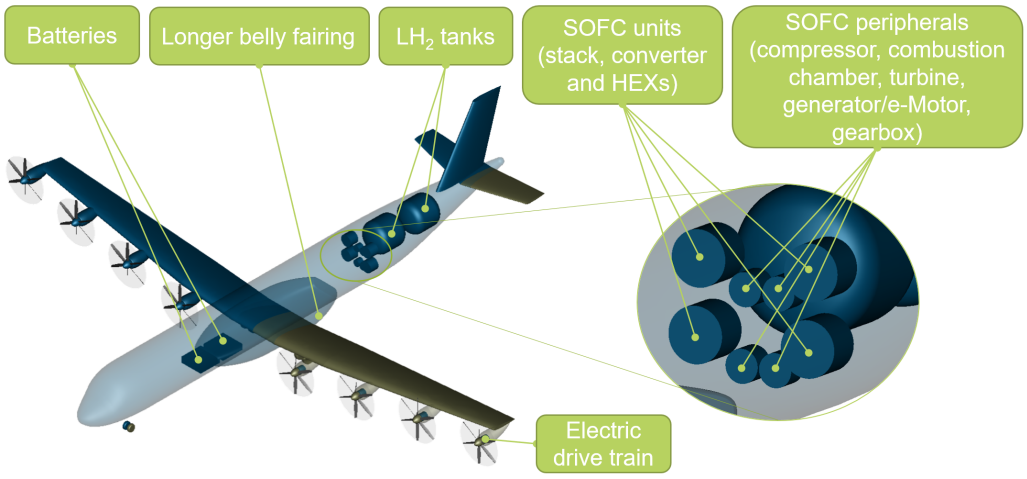


Figure 13 – Powertrain integration for the fuselage-integrated configuration.

Figure 13 shows the powertrain integration for the FI-configuration. When comparing this integration with the one of the NI-configuration in Figure 10, it can be observed that both architectures share the location of the liquid hydrogen tanks in the rear of the fuselage, of the batteries out of the propeller disc plane in the elongated belly fairing, and the location of the electric drive train in the nacelles. The difference lies in the placement of the SOFC system. In the FI-configuration, the location chosen is at the rear of the fuselage, behind the cabin pressure bulkhead and in front of the hydrogen tanks. This decision was made for safety reasons, to position the propulsion components as far away from the passengers as possible and to create sufficient vertical space for a crash structure. For these reasons, the location at the rear of the fuselage was preferred over a potential integration within the belly fairing. Moreover, only four SOFC units are shown in Figure 13. This does not indicate that only half the power is installed for this configuration compared to the nacelle-integrated one. Instead, more cells are incorporated per unit relative to ones in the nacelles.

Parameter	Unit	Nacelle Integrated	Fuselage Integrated
MTOM	kg	23080	21950
OEM	kg	18080	17075
PAX	-	48	48
Max. Payload	kg	4700	4700
Wing area	m^2	68.7	65.5
Aspect ratio	-	14	14
Design Range	NM	740	740
Cruise Ma	-	0.4	0.4
Cruise altitude	ft	24000	24000
L/D mid cruise	-	19.3	20.1

Table 4 – Key data of the SOFC-powered aircraft.

3.3 Mass breakdown comparison

Figure 14 depicts the aircraft mass comparison of the two SOFC-powered aircraft concepts with the baseline. The OEM shows a significant increase for the SOFC-powered aircraft which can be attributed to the heavier powertrain. Figure 15 shows the mass breakdown of the powertrain for the three regarded aircraft. SOFC stack and battery jointly exceed the mass of the entire baseline's powertrain. This mass increase is only slightly alleviated by the reduced fuel mass due to the higher gravimetric energy density of hydrogen compared to kerosene. The design payload of the SOFC-powered aircraft and the baseline is identical with 4560 kg.

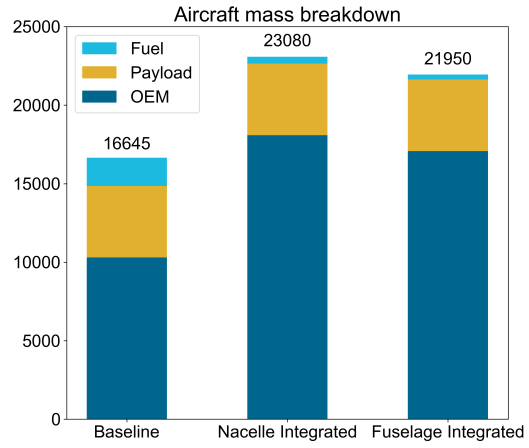


Figure 14 – Aircraft mass comparison.

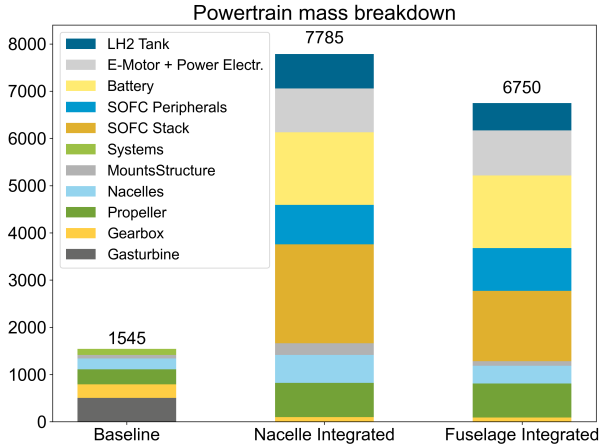
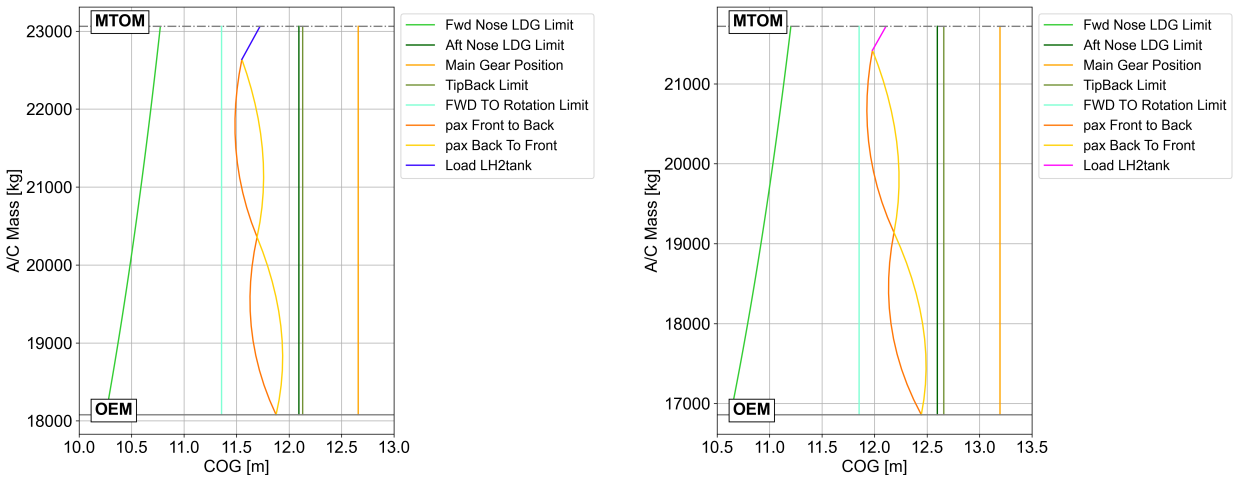


Figure 15 – Powertrain mass comparison.

When comparing the two SOFC-powered aircraft concepts, the FI-concept is lighter than the NI-concept. This is primarily due to the more efficient powertrain integrated into this concept utilizing more turbine power because of the included gearbox and electric generator as well as including a hydrogen recirculation. Therefore, the power requirement for the SOFC is reduced leading to lighter components and less hydrogen consumption which in turn reduces the size and mass of the liquid hydrogen tanks. Thus, the lower mass of the FI-concept compared to the NI-concept is primarily driven by the lower mass of the SOFC stack and the LH_2 tanks which is reflected in Figure 15. The smaller and therefore lighter nacelles of the FI-configuration have another reducing effect on the powertrain mass. However, this has to be considered alongside the mass impact of the longer fuselage of that configuration which is not shown separately in Figure 15 but attributed to the OEM in Figure 14.

3.4 Weight and Balance



(a) Nacelle integrated.

(b) Fuselage integrated.

Figure 16 – Weight and Balance of the SOFC-powered aircraft.

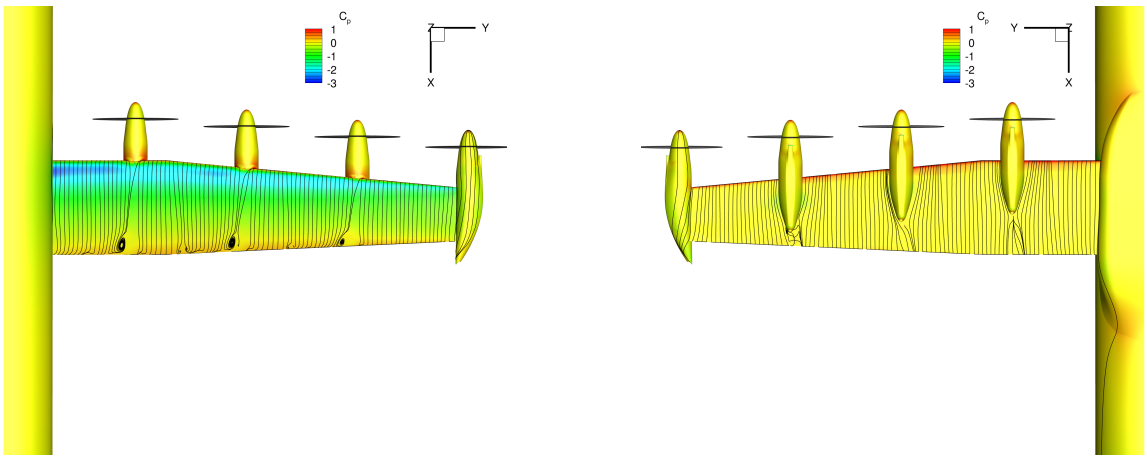
The system integration shown in Figure 10 and Figure 13 reveals that the position of the batteries differs. The batteries in the NI-concept are located behind the wing in the lower fuselage, whilst those in the FI-concept are positioned in front of the wing. The reason for this lies in the weight-and-balance assessment. As the masses of the powertrain in the FI-concept are located further away from the center of gravity in the rear section of the fuselage, less margin is available for this concept regarding loading and center of gravity shift. To mitigate the risk of exceeding these limits, the batteries in front of the wing help to offset the weight of the SOFC system in the rear section of the fuselage, thereby shifting the center of gravity and thus the wing forward. This in turn increases the margin for the forward rotation limit, as the lever arm of the horizontal stabilizer relative to the main wing is now greater. This allows the passenger cabin to remain fully loaded, which was not possible with the batteries arranged behind the wings. The resulting WAB-diagrams are presented in Figure 16. From a WAB perspective, the NI-concept presents no issues. As the main masses of the powertrain are located in the nacelles underneath the wings, they are close to the center of gravity, which reduces the risk of reaching a rotation or pitch limit.

3.5 Aerodynamics

The assessment of the aero-propulsive performance was performed at mid-cruise conditions with balanced drag and is based on an intermediate aircraft design and applied to the final results. Table 5 gives a summary of these conditions. Therefore, for each configuration the blade pitch angles were adjusted until the overall thrust equals the configuration's total drag. Figure 17 depicts the surface pressure distribution and the skin friction lines of the nacelle-integrated configuration. In this case, the angle of attack is $\alpha = 0.4°$. The suction peak on the upper side of the wing is strongest at the wing root and decreasing towards the tip as shown in Figure 17a. The rather low loading on the outboard wing was a design decision to prevent premature flow separation at low-speed conditions [34]. Moreover, the plot reveals generally lower surface pressure in the inboard regions of the nacelles compared to the outboard region, which is caused by the propeller swirl with an inboard up rotation. The skin friction lines indicate local trailing edge flow separation downstream of the nacelles. On the lower side of the wing, the skin friction lines hint at rotational flow behind nacelle 1 and a larger recirculation area downstream of nacelle 3 as shown in Figure 17b.

Parameter	Unit	Value
Height	m	7315.2
Reference density	kg/m^3	0.5692
Freestream Mach number	-	0.4
Lift coefficient	-	0.733

Table 5 – Flow conditions for RANS simulations.



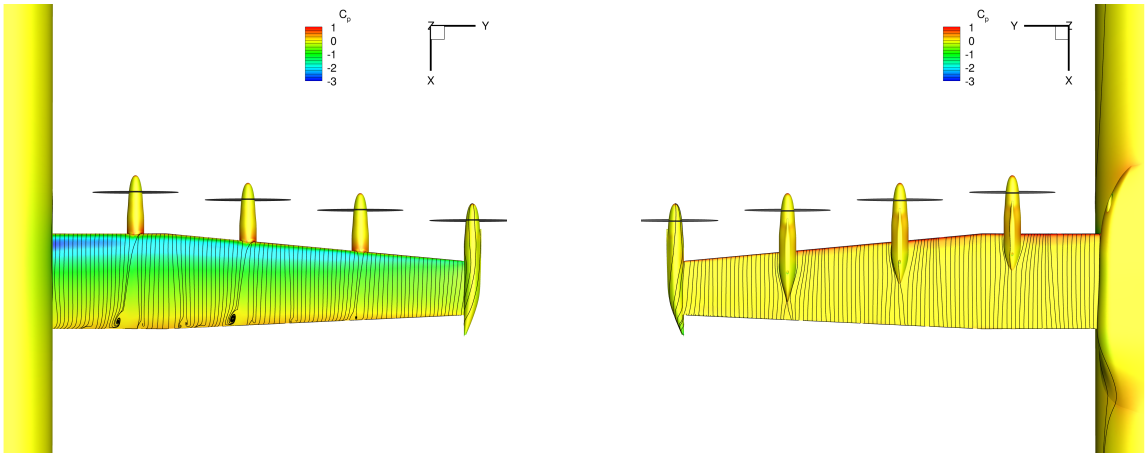
(a) Upper side (b) Lower side

Figure 17 – Surface pressure distribution and skin friction lines of the nacelle-integrated concept at mid cruise conditions, propellers on.

The total airframe drag coefficient – including fuselage, wing, tail, and nacelles – is $C_D = 0.0394$ in the

case without propeller effects. The beneficial effects of the propeller slipstream on the drag distribution result in a reduction of induced drag and thus pressure drag. Despite increased flow separation, the pressure drag is reduced by $\Delta C_{D,p} \approx -0.0008$ compared to the case without propeller effects. Consequently, the friction drag increase of $\Delta C_{D,f} = 0.0002$ caused by the propeller effects is more than compensated for. As a result, considering propeller effects yield a total airframe drag coefficient of $C_D = 0.0389$. Due to the high pressure and temperature of the gas coming from the power train, the effect of internal flow related to the power train is beneficial to the drag balance. The forces of the internal airflow to and from the fuel cell can be determined based on the inlet and outlet boundary conditions at the nacelles. In the case with propeller effects, this results in an internal drag of $\Delta C_D \approx -0.0006$, reducing the total drag coefficient to $C_D \approx 0.0383$.

Figure 18 depicts the surface pressure distribution and skin friction lines of the fuselage-integrated configuration. Compared to the nacelle-integrated configuration, the angle of attack that is necessary to achieve the mid-cruise lift coefficient is slightly higher with $\alpha = 0.9°$. Similar to the nacelle-integrated configuration, also the fuselage-integrated configuration shows local trailing edge flow separation downstream of the nacelles as depicted in Figure 18a. However, these regions are notably reduced compared to the nacelle-integrated configuration. Figure 18b shows the lower side of the wing. Here, the skin friction lines indicate that the air flows smoothly over the wing. The airframe drag coefficent yields $C_D = 0.0374$. Again, considering the internal forces, the drag coefficient is reduced to $C_D = 0.0366$.



(a) Upper side (b) Lower side

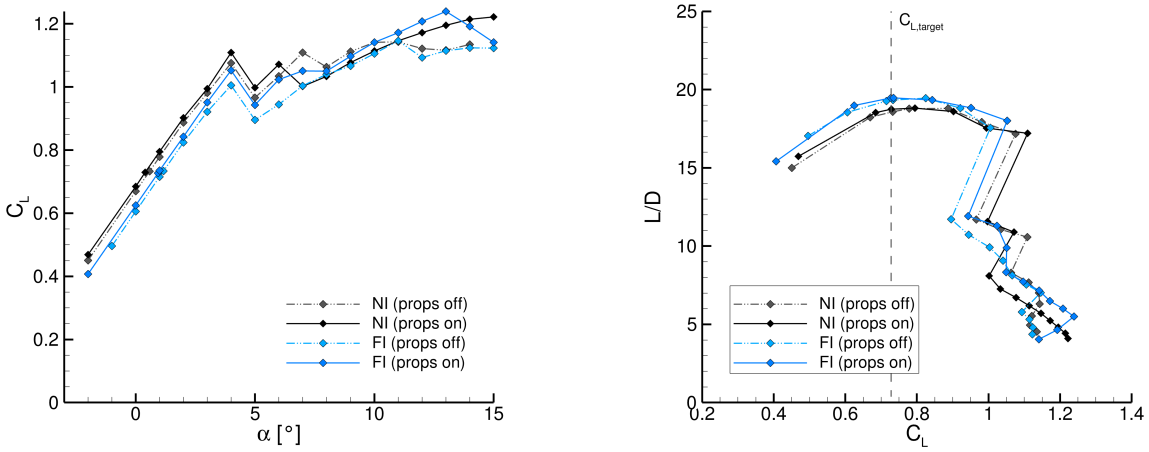
Figure 18 – Surface pressure distribution and skin friction lines of fuselage-integrated concept at mid cruise conditions, propellers on.

Figure 19a compares the lift curves of the two concepts, with and without propeller effects. It shows that, in the linear range and at the same angle of attack, the lift of the NI-concept is approximately $\Delta C_L = 0.06$ higher than the one of the FI-concept. Both variants show an initial drop in the lift curve at $\alpha = 5°$, caused by local flow separation in the wing root region. The lift coefficient then continues to rise, however, until nacelle-induced flow separation limits the maximum lift coefficient in the case of the FI-configuration with and without propeller effects, and the NI-configuration without propeller effects. In contrast, the maximum lift coefficient is limited by local flow separation between the two central propellers (propellers 2 and 3) in the case of the NI-configuration with propeller effects. Figure 19b compares the glide ratio of the two concepts as a function of the lift coefficient. It shows that the FI-concept has a higher L/D in the linear range at

Parameter	Unit	NI	FI
Alpha	°	0.4	0.9
Thrust	kN	5.48	5.37
L/D	-	18.84	19.63
η_{prop}	%	89.6	89.6

Table 6 – Summary of aero-propulsive performance.

same lift coefficients. At the mid cruise flight level, the L/D of the FI-concept is 4 % higher than the one of the NI-concept. In contrast, the type of propulsion integration has no influence on the average propeller efficiency. Table 6 summarizes the key aero-propulsive performance metrics.



(a) Lift coefficient

(b) Lift-to-drag ratio

Figure 19 – Comparison of lift coefficient and L/D in cruise flight between nacelle-integrated and fuselage-integrated concepts.

3.6 Mission performance

The power usage comparison in Figure 20 underlines the positive effects of the FI-concept incorporating the advanced powertrain resulting in less energy consumption and a reduced overall aircraft mass compared to the NI-concept. Here the power drawn from the SOFC and the battery over the mission is shown. The NI-configuration (green) demands more power of the SOFC over the entire mission than the FI-concept (blue). Also, the battery has to deliver more power during take-off and go-around. Moreover, the buffering effect of the battery can be seen clearly. Only during take-off and go-around the battery delivers additional power while no power is drawn during cruise. In the descent phases the battery is charged again by excess power of the SOFC. The battery of the NI-concept is charged proportional to the higher power of the SOFC for this configuration.

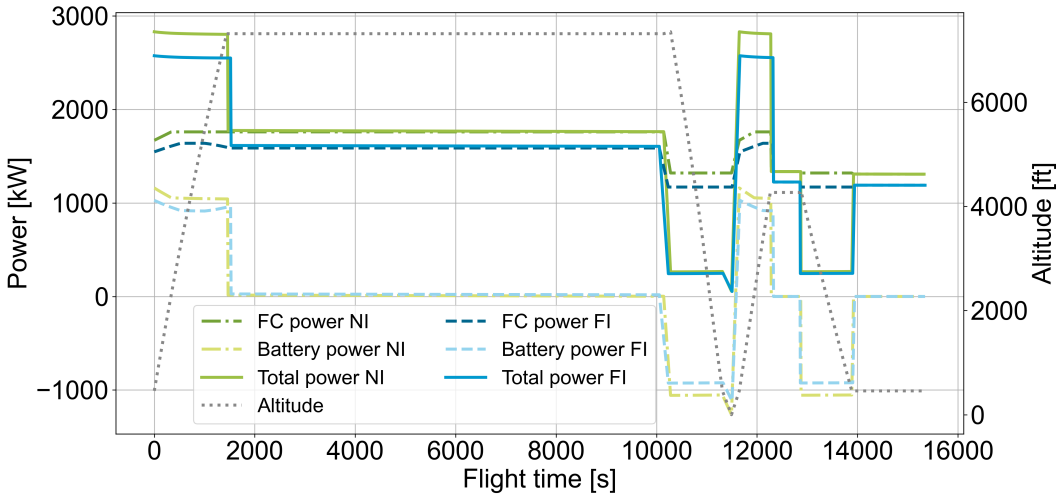
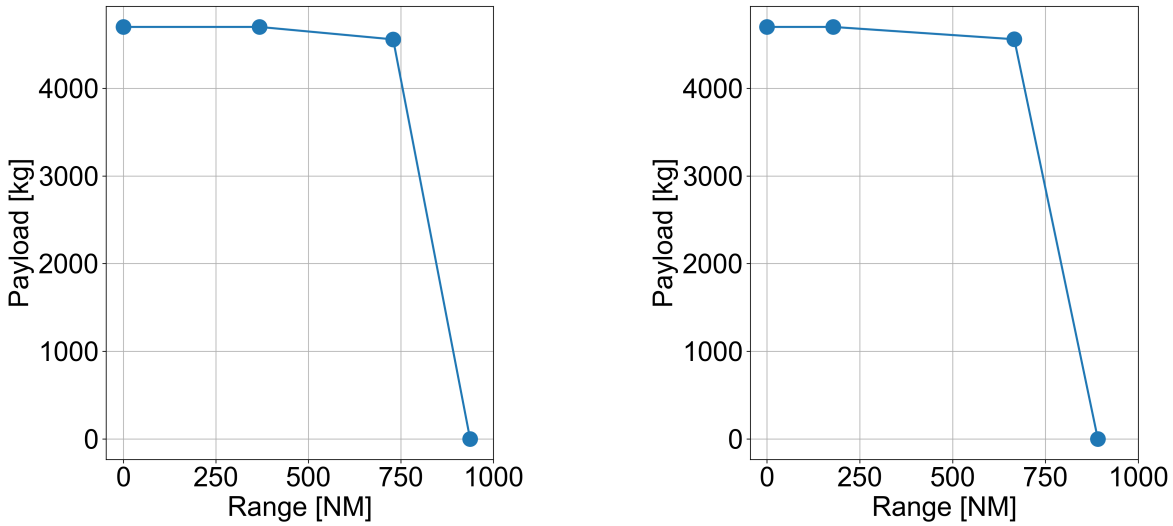


Figure 20 – Power usage comparison over the design mission.

The payload-range diagrams in Figure 21 show the typical behavior of hydrogen-powered aircraft with a substitution line shallower than one of an aircraft powered by hydrocarbon fuel. This is due to the higher gravimetric energy density of hydrogen resulting in less mass decrease over the mission.

Hence the difference between maximum payload and design payload decreases. In order to keep the design point of the SOFC aircraft close to the one of the baseline in an economical viable range, which is transporting the same maximum amount of passengers over a range of 700 to 800 NM, the maximum payload of the SOFC aircraft is reduced to 4700 kg. The design mission in Figure 7, which the SOFC aircraft are optimized for, reproduces this behavior. Typical missions of regional aircraft are around 200 to 300 NM. Both missions – design and typical – can be flown by the SOFC aircraft as can be seen in both payload-range diagrams. Hence, to not oversize and as a consequence penalize the SOFC aircraft, the maximum payload is reduced to achieve a fair comparison between baseline and SOFC aircraft regarding its operation.



(a) Nacelle integrated.

(b) Fuselage integrated.

Figure 21 – Payload-Range diagrams of the SOFC aircraft.

The substitution line between the middle two points of the payload-range diagrams in Figure 21 shows again the higher efficiency of the FI-concept compared to the NI-concept. The slope of the substitution line of the FI-concept is shallower than the one of the NI-concept which indicates a higher efficiency. The greater range with maximum payload achieved by the NI-concept is a result of more installed power due to its higher mass.

3.7 Block Energy Comparison

Figure 22 provides a cruise efficiency and block energy comparison for the SOFC-powered aircraft and the baseline. For this comparison all aircraft are evaluated using the same mission depicted in Figure 7 – cruising at 24000 ft with a cruise Mach number of 0.4 over a range of 740 NM.

As shown in more detail in Section 3.3, the SOFC aircraft reveal a significant mass increase. At the mid cruise point, the NI-configuration shows a mass increase of 43 % and the FI-configuraton 37 % compared to the baseline which is attributable to the greater mass of the powertrain. Nevertheless, the lift-to-drag (L/D) ratio of the SOFC-powered aircraft improves by 9 % and 14 %, respectively, which can be explained by the larger span and generally greater wing area these aircraft have compared to the baseline. The higher L/D of the FI- compared to the NI-configuration is due to the smaller nacelles which results in less flow separation and therefore less drag as described in Section 3.5. The improved L/D ratio alleviates the impact the increased mass has on cruise performance. Thus, the required thrust for the SOFC-powered aircraft at mid cruise increases by 31 % and 22 % with respect to the baseline. The slight difference in the L/D-data here and in Section 3.5 are the result of an aspect ratio variation. The final results have a higher aspect ratio compared to the intermediate aircraft design used for the CFD-analyses.

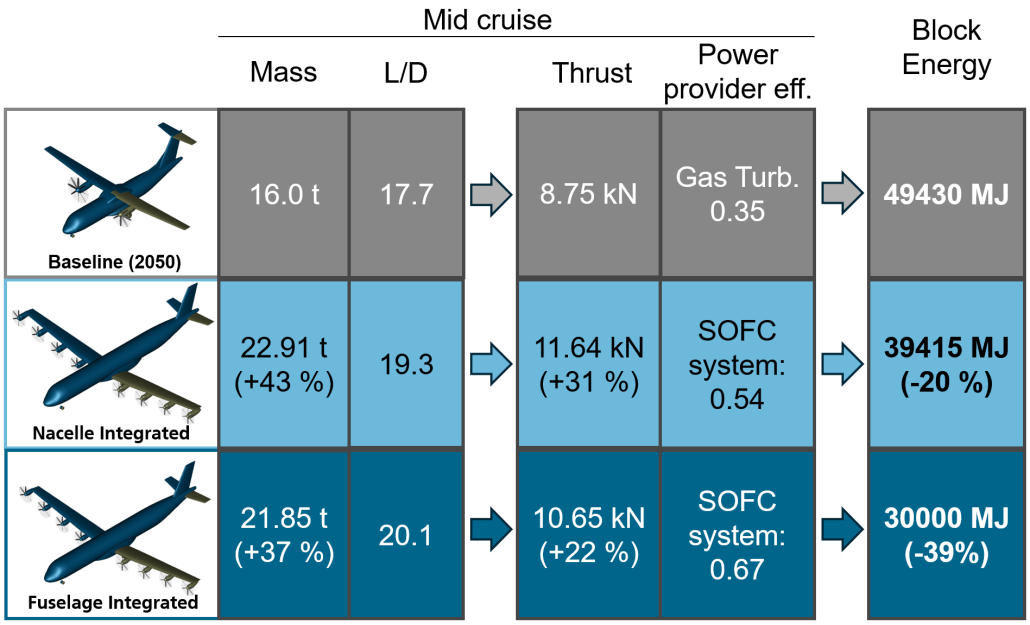


Figure 22 – Mid cruise point comparison and block energy usage of the baseline, NI- and FI-concept.

A comparison of block energy efficiency shows that the NI-concept is around 20 % more efficient, and the FI-concept is around 40 % more efficient than the baseline concept despite the higher thrust required during cruise. Both can be attributed to a more efficient powertrain compared to the gas turbines installed on the baseline. In mid-cruise condition the powertrain of the NI-configuration achieves an overall efficiency of 54 %, the more sophisticated powertrain of the FI-configuration with its improved turbine utilization reaches 67 %. Considering solely the SOFC-concepts, it can be seen that the FI-concept is around 24 % more efficient than the NI-concept.

3.8 Study on Gravimetric Power Density

The previous results, especially the block energy comparison in Section 3.7 yielding up to 40 % improvement compared to an aircraft that has already undergone evolutionary improvements, are promising for the use of SOFC in aviation. However, these results are based on rather optimistic assumptions for the SOFC which, although already been demonstrated in the laboratory, have not yet been tested in real-world applications. Nevertheless, it is of interest what different assumptions concerning the gravimetric power density have on overall aircraft level. The integration of the SOFC-powertrain sizing into the aircraft design workflow now allows individual powertrain parameters and assumptions to be adjusted, with the resulting impact being assessed on the overall aircraft level. Therefore, the workflow from Section 2.1 is applied reducing the assumption for the gravimetric power density of the SOFC to identify a breakeven point with the baseline concerning the block energy. The reduction in gravimetric power density is accompanied by a larger volume of the SOFC stack, which also increases the length of the fuselage. An extension in radial direction is excluded in order to keep the fuselage diameter constant and to ensure comparability with the previous results. The basic shape of the wing is also kept the same. Only an adjustment in spanwise direction and of the chord is possible. Due to the higher mass of the SOFC stacks, the take-off mass increases as well which in turn raises the power requirement of the powertrain. This is taken into account by the use of the workflow whereby the remaining components of the powertrain are adapted to the specific power density of the SOFC. In the synthesis, a comparison with the block energy of the baseline is conducted. The gravimetric power density is reduced until the block energy of the SOFC aircraft matches the one of the baseline. Hence, the block energy serves as further convergence criterion.

Preliminary studies have shown that below a gravimetric power density of 1000 W/kg, the wingspan exceeds the ICAO gate limit of 36 m, which is typically used by short and medium range aircraft

like the Airbus A320. For this reason, the wingspan was limited to 36 m. An increase in wing area is then only possible by extending the chord. Due to the larger span, it is possible to extend the propeller diameter in order to increase the entire disc area and thus the propeller efficiency. The side-clearance, a reduction in rotational speed of the propellers and an increase in gearbox mass due to the increased torque are also taken into account.

Figure 23 shows the exponential increase of the block energy for the mission in Figure 7 over the reduction of the gravimetric power density of the SOFC. The breakeven point with the block energy of the baseline is reached at a power density of 450 W/kg. Compared with the current state of the art for SOFC assemblies and stacks reaching 100 to 300 W/kg, this is an increase of 150 % to 450 %. Tew et al. [9] issues a target value of 700 W/kg for single-aisle aircraft, whereby short and medium range aircraft were probably assumed here. Therefore, the result of this study for regional aircraft seems to fit this target.

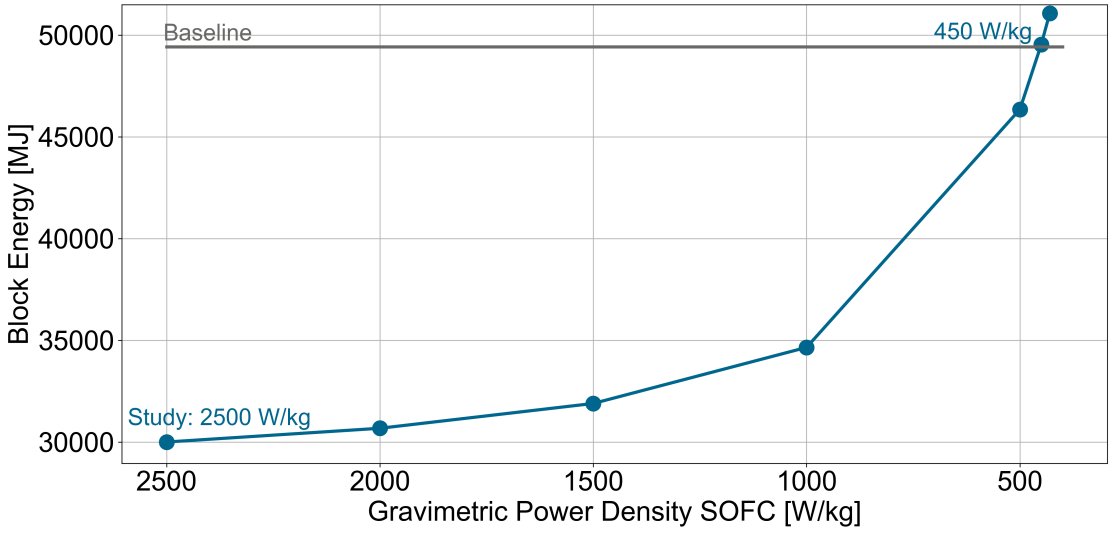
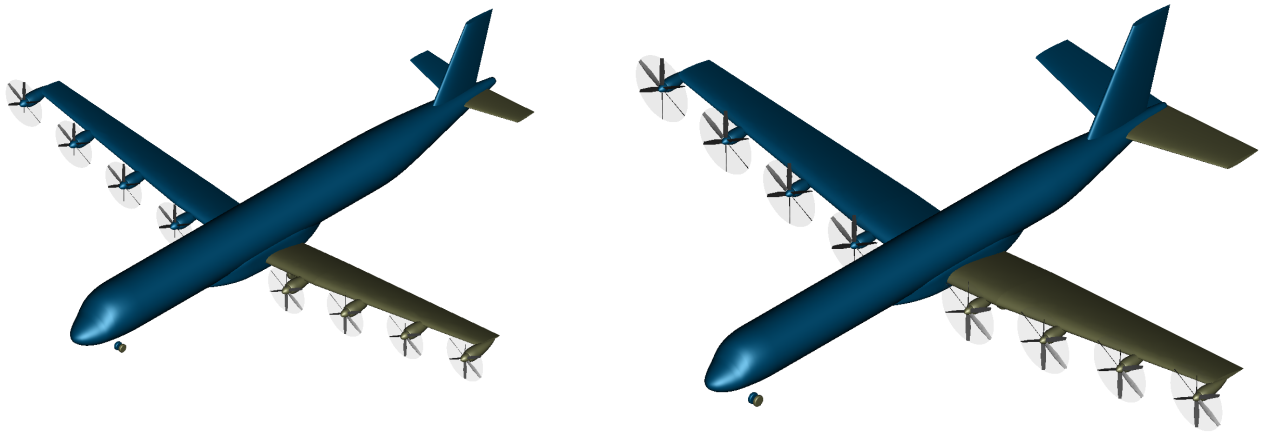


Figure 23 – Results of the gravimetric power density-study for the example of the FI-configuration.

Figure 24 depicts an isometric view of the FI-configuration with 2500 W/kg and the one with 450 W/kg, showcasing the effect a reduction in gravimetric power density of the SOFC has on aircraft level. Salient is the significantly larger empennage and the aftward shift of the wing position of the aircraft with reduced SOFC gravimetric power density. Table 7 shows a comparison of key data of these two aircraft and the baseline. The powertrain mass increases by a factor of about 2.4 most of which is attributed to the SOFC system in the aft of the aircraft behind the cabin pressure bulk head and in front of the hydrogen tanks. Consequently, the CoG of the aircraft shifts backwards and thus, the wing position. Therefore, the lever arm of the empennage to the CoG is reduced resulting in significantly larger surface areas of the horizontal and vertical stabilizer. Due to the substantial higher powertrain mass, the operating empty mass (OEM) and the maximum take-off mass (MTOM) increase as well. Consequently, also the wing area increases to achieve the required lift. The wing span is kept at 36 m but the propeller diameter increased from 2.5 to 3.5 m. The ICAO gate limit, however, can be complied with by introducing foldable blades for the wing-tip propellers. The fuselage length is increased as well due to the larger volume of the SOFC stacks and the stated restriction of keeping the fuselage diameter constant.

Compared to the baseline, the increase in mass and overall dimensions are even more significant. The OEM increases by a factor of 3.4 and the wing area more than doubles for the aircraft with a gravimetric power density of 450 W/kg. These results show the theoretical feasibility of an aircraft powered by an SOFC powertrain with a gravimetric power density of 450 W/kg. However, the considerable challenges also become evident. Moreover, the design kept the high efficiency of 67 % of the

powertrain and the design is based on a reduction in cruise Mach number to 0.4 compared to current state-of-the-art regional aircraft to lower the propulsion power required. Therefore, a gravimetric power density of 450 W/kg of the SOFC stack is considered the absolute lower limit for a regional aircraft in terms of energy demand.



(a) FI 2500 W/kg. (b) FI 450 W/kg.

Figure 24 – ISO-views of the aircraft in the gravimetric power density-study.

Parameter	Unit	Baseline	FI 2500 W/kg	FI 450 W/kg
MTOM	kg	16645	21950	40160
OEM	kg	10295	17075	35135
Powertrain mass	kg	1545	6750	16050
Wing area	m^2	54.6	65.5	118.5
Wing span (+prop)	m	27.6	32.8	39.5
Fuselage length	m	22.7	29.0	30.9

Table 7 – Key data of the FI-concept with different SOFC gravimetric power density-ratios compared to the baseline.

4. Conclusion

This study examines the viability of an SOFC propulsion system for long-term application in a regional aircraft. Therefore, a sizing workflow is set up consisting of several tools and routines covering conceptual aircraft design and more specialized disciplines like the SOFC-powertrain sizing and aerodynamic analysis. Using this design process, two SOFC-powered aircraft concepts are designed, one with the SOFC system integrated into the aircraft's nacelles and one with the SOFC system integrated into the fuselage. Thereby also two powertrain architectures are introduced. One architecture with less components to fit into the nacelles and one architecture with a more sophisticated layout located in the rear fuselage. These two SOFC powered concepts are point designs resulting from the assumption of an SOFC gravimetric power density of 2.5 kW/kg and a battery energy density of 500 Wh/kg. The SOFC-powered aircraft are analyzed concerning powertrain integration, mass, aerodynamics mission performance and block energy consumption. Compared to a baseline, representing an evolutionary enhanced conventional aircraft for the year 2050 powered by gas turbines and hydrocarbon fuel, the most favorable SOFC-powered aircraft with a fuselage-integrated SOFC system shows a significant efficiency improvement of about 40 % block energy reduction. Given these large improvements and the rather optimistic assumptions for the SOFC, a sensitivity analysis is conducted concerning the gravimetric power density of the SOFC. This aimed for identifying the minimum required gravimetric power density an SOFC has to achieve in order for the aircraft equipped with such a powertrain to reach a break-even with the baseline in terms of block energy required. A minimum gravimetric power density of 450 W/kg is identified for the FI-concept requiring the

same block energy as the baseline. Compared with the FI-concept with an SOFC gravimetric power density of 2500 W/kg and also compared to the baseline, the SOFC aircraft with the gravimetric power density reaching the break-even point shows a significant increase in mass, more than doubling the OEM. Furthermore, the wingspan has to be limited as well in order to not exceed the ICAO gate limit of 36 m for short- and medium-range aircraft. Consequently, an SOFC gravimetric power density of 450 W/kg is regarded as the absolute minimum required to power a regional aircraft using this type of fuel cell. For a real-world application, the SOFC would need to be further improved significantly in order for an aircraft manufacturer to justify the additional development costs of an SOFC-powered regional aircraft compared to a conventionally advanced one.

The findings show that a powertrain, despite having more components and thus potentially adding more weight, can result in an aircraft lighter and significantly more efficient than an aircraft equipped with a powertrain comprising fewer components. This opens up more detailed research opportunities. Future work could focus on further optimizing the integration of the more sophisticated SOFC powertrain. For example, this powertrain can be partly integrated into the nacelles to obtain a greater margin concerning the limits in the weight-and-balance. Moreover, aeroelastic analyses are needed for wings with distributed propulsion and heavy components integrated into the nacelles. Finally, the integration of an analysis regarding the direct operating costs of an SOFC-powered aircraft, establishing a breakeven point not only from an energy, but also from an economical perspective, could significantly contribute to a more comprehensive evaluation of the feasibility of commercially viable SOFC-powered aircraft.

5. Contact Author Email Address

Nicolas Schneiders
German Aerospace Center (DLR)
Institute of System Architectures in Aeronautics, Hamburg, Germany
nicolas.schneiders@dlr.de

6. Copyright Statement

The authors confirm that they, and/or their company or organization, hold copyright on all of the original material included in this paper. The authors also confirm that they have obtained permission, from the copyright holder of any third party material included in this paper, to publish it as part of their paper. The authors confirm that they give permission, or have obtained permission from the copyright holder of this paper, for the publication and distribution of this paper as part of the ICAS proceedings or as individual off-prints from the proceedings.

References

[1] Gopalasingam D., Rakhshani B., and Rodriguez C. Hydrogen Propulsion Technologies for Aviation: A Review of Fuel Cell and Direct Combustion Systems Towards Decarbonising Medium-Haul Aircraft. *Hydrogen*, 6(4):92, 2025.

[2] Koops L. Technologies on the Radar – Signals for Innovation Potentials in Fuel Cells and Batteries for Electric Flight. In *Deutscher Luft- und Raumfahrtkongress 2025*, Augsburg, 2026.

[3] Kazula S., de Graaf S., and Enghardt L. Review of fuel cell technologies and evaluation of their potential and challenges for electrified propulsion systems in commercial aviation. *Journal of the Global Power and Propulsion Society*, 7:43–57, 2023.

[4] Borup R., Meyers J., Pivovar B., Kim Y. S.and Mukundan R., Garland N., Myers D., Wilson M., Garzon F., Wood D., Zelenay P., More K., Stroh K., Zawodzinski T., Boncella J., McGrath J. E., Inaba M., Miyatake K., Hori M., Ota K., Ogumi Z., Miyata S., Nishikata A., Siroma Z., Uchimoto Y., Yasuda K., Kimijima K.-I., and Iwashita N. Scientific Aspects of Polymer Electrolyte Fuel Cell Durability and Degradation. *Chemical reviews*, 107(10):3904–3951, 2007.

[5] Marciello V., Di Stasio M., Ruocco M., Trifari V., Nicolosi F., Meindl M., Lemoine B., and Caliandro P. Design Exploration for Sustainable Regional Hybrid-Electric Aircraft: A Study Based on Technology Forecasts. *Aerospace*, 10(2):165, 2023.

[6] Steffen Jr. C. J., Freeh J. E., and Larosiliere L. M. Solid Oxide Fuel Cell/Gas Turbine Hybrid Cycle Technology for Auxiliary Aerospace Power. Technical report, Glenn Research Center, 2005.

[7] McPhail S. J., Leto L., and Bolgues-Munez C. *The Yellow Pages of SOFC Technology: International Status of SOFC deployment 2012-2013: IEA - Implementing Agreement Advanced Fuel Cells Annex 24 – SOFC*. ENEA National Agency for New Technologies, Energy and Sustainable Economic Development, 2013.

[8] Moritz G. Kolb, A. Seitz, and M. Hornung. Single gas turbine propulsion options for short-to-medium range aircraft. *Proceedings of Global Power and Propulsion Society*, 2025.

[9] Tew D. E., Cox-Galhotra R. A., Lecoustre V. R., Lyubovsky M., and Soloveichik G. L. Perspective—The Role of Solid Oxide Fuel Cells in Our Carbon-Neutral Future. *Journal of The Electrochemical Society*, 169(2):024508, 2022.

[10] Whyatt GA. and Chick LA. Electrical generation for more-electric aircraft using solid oxide fuel cells. Technical report, Pacific Northwest National Laboratory, 2012.

[11] Santarelli M., Cabrera M., and Calì M. Analysis of Solid Oxide Fuel Cell Systems for More-Electric Aircraft. *Journal of Aircraft*, 46(1):269–283, 2009.

[12] Seitz A., Nickl M., Troeltsch F., and Ebner K. Initial Assessment of a Fuel Cell—Gas Turbine Hybrid Propulsion Concept. *Aerospace*, 9(2):68, 2022.

[13] Waters D. F. and Cadou C. P. Engine-integrated solid oxide fuel cells for efficient electrical power generation on aircraft. *Journal of Power Sources*, 284:588–605, 2015.

[14] Collins J. M. and McLarty D. All-electric commercial aviation with solid oxide fuel cell-gas turbine-battery hybrids. *Applied Energy*, 265:114787, 2020.

[15] Pascal Köhler, Jan Hollmann, Anis Taissir, Marc P. Heddrich, and Stephan Kabelac. Future Highly Efficient Engines with Solid Oxide Fuel Cell–Gas Turbine Coupling: System Modeling Study and Comparison of Directly and Indirectly Coupled SOFC–Gt Systems. *Aerospace*, 13(3):263, 2026.

[16] Kierbel D., Neuland T., Roux P.-E., Nehter P., Hollmann J., Dagli C. N., Koehler P., Kabelac S., Rao A. G., de Domenico F., Hoogreef M., Van Biert L., Yin F., Rossignol C., Dessemond L., Steil M. C., Maas P., Winter F., Warsch C., Ventura S. S., Metten M., Heddrich M. P., and Asif Ansar S. HYLENA project (HYdrogen eLectrical Engine Novel Architecture) Hydrogen-Powered Solid Oxide Fuel Cell -Gas Turbine System for Aeronautical Application. In *ICAS Proceedings: 34th Congress of the International Council of the Aeronautical Sciences*, Florence, Italy, 2024.

[17] Boden B., Flink J., Först N., Mischke R., Schaffert K., Weinert A., Wohlan A., and Schreiber A. RCE: An Integration Environment for Engineering and Science. *SoftwareX*, 15:100759, 2021.

[18] M. Alder, E. Moerland, J. Jepsen, and B. Nagel. Recent Advances in Establishing a Common Language for Aircraft Design with CPACS. In *Aerospace Europe Conference, Bordeaux, France, 25–28 February 2020*, 2020.

[19] Wöhler S., Atanasov G., Silberhorn D., Fröhler B., and Zill T. Preliminary Aircraft Design within a Multidisciplinary and Multifidelity Design Environment. In *Aerospace Europe Conference, Bordeaux, France, 25–28 February 2020*, 2020.

[20] Bahrs V. J., Franke F., Kazula S., and de Graaf S. Analysis of the potential of metal hydride-based range extenders for electric commuter aircraft. *CEAS Aeronautical Journal*, 16(1):255–273, 2025.

[21] Burschyk T., Fröhler B., Alder M., and Zill T. Global Sensitivity Analysis of Liquid Hydrogen Storage Design Parameters for Overall Aircraft Design. In *ICAS Proceedings: 34th Congress of the International Council of the Aeronautical Sciences*, Florence, Italy, 2024.

[22] Freund S., Burschyk T., Jacobsen L., and Franzoni F. Automated structural design optimization of double walled liquid hydrogen tanks and comparison of cfrp with aluminium on aircraft level. In *DLRK 2025*, Augsburg, Germany, 2025.

[23] Thomas Gerhold. Overview of the Hybrid RANS Code TAU. In Kroll N. and Fassbender J. K., editors, *MEGAFLOW - Numerical Flow Simulation for Aircraft Design*, pages 81–92, Berlin, Heidelberg, 2005. Springer Berlin Heidelberg.

[24] Spalart P. and Allmaras S. A one-equation turbulence model for aerodynamic flows. In *30th Aerospace Sciences Meeting and Exhibit*, Reston, Virigina, 1992. American Institute of Aeronautics and Astronautics.

[25] P.R. Spalart and M. Shur. On the sensitization of turbulence models to rotation and curvature. *Aerospace Science and Technology*, 1(5):297–302, 1997.

[26] Raichle A. Flux Conservative Discretization of the Actuator Disk Model as a Discontinuity Surface. Ph.d. thesis, Technical University Braunschweig, Braunschweig, Germany, 2017.

[27] Raichle A., Melber-Wilkending S., and Himisch J. A new Actuator Disk Model for the TAU Code and application to a sailplane with a folding engine. In *New Results in Numerical and Experimental Fluid Mechanics VI: Contributions to the 15th STAB/DGLR Symposium Darmstadt, Germany*, volume 96. Springer

Berlin Heidelberg, 2008.

[28] Lenfers C., Beck N., and Bauer M. Propeller and Active High Lift Wing Interaction in Experiment and Simulation. *New Results in Numerical and Experimental Fluid Mechanics X*, 132:51–61, 2016.

[29] Márquez Gutiérrez C., Stuermer A., Clemen C., and Grimminger A. Validation of actuator disk simulations of cror propulsion systems at low-speed flight conditions. In *30th AIAA Applied Aerodynamics Conference*, Reston, Virigina, 2012. American Institute of Aeronautics and Astronautics.

[30] ATR. ATR 42-500 A New Standard of Excellence, 2005.

[31] ATR. ATR Evo Concept. `https://www.atr-aircraft.com/innovation/atr-evo-concept/`. Accessed: 30.04.2026.

[32] Link A. and de Graaf S. Projection of key powertrain component figures of merit for overall assessment of electric flight scenarios. In *ICAS Proceedings: 34th Congress of the International Council of the Aeronautical Sciences*, Florence, Italy, 2024.

[33] ATR. ATR 42-600: The ideal local commuter.

[34] Keller D., Visingardi A., Wiart L., Maldonado Y.-B., and Morlando F. Aerodynamic investigation of a propeller-driven transport aircraft with distributed propulsion within the imothep project. In *9th European Congress on Computational Methods in Applied Sciences and Engineering, ECCOMAS 2024, 3-7 June 2024, Lisbon, Portugal*, 2024.